Chemistry–A European Journal
Research Article
doi.org/10.1002/chem.202401797
Chemistry Europe
European Chemical Societies Publishing
www.chemeurj.org

Exploring the Esterase Catalytic Activity of Minimalist Heptapeptide Amyloid Fibers

L. Roldan,[a] L. Rodríguez-Santiago,*[a] J. Didier-Marechal,[a] and M. Sodupe*[a]

This paper investigates the esterase activity of minimalist amyloid fibers composed of short seven-residue peptides, IHIHIHI (IH7) and IHIHIQI (IH7Q), with a particular focus on the role of the sixth residue position within the peptide sequence. Through computational simulations and analyses, we explore the molecular mechanisms underlying catalysis in these amyloid-based enzymes. Contrary to initial hypotheses, our study reveals that the twist angle of the fiber, and thus the catalytic site's environment, is not notably affected by the sixth residue. Instead, the sixth residue interacts with the p-nitrophenylacetate (pNPA) substrate, particularly through its $-NO_2$ group, potentially enhancing catalysis. Quantum mechanics/molecular mechanics (QM/MM) simulations of the reaction mechanism suggest that the polarizing effect of glutamine enhances catalytic activity by forming a stabilizing network of hydrogen bonds with pNPA, leading to lower energy barriers and a more exergonic reaction. Our findings provide valuable insights into the intricate interplay between peptide sequence, structural arrangement, and catalytic function in amyloid-based enzymes, offering potentially valuable information for the design and optimization of biomimetic catalysts.

Introduction

Amyloids fibrils are ordered nanostructures resulting from the self-assembly of amyloid proteins. Although they have been traditionally associated as the end product of pathological misfolding in several human diseases,[1] recent discoveries have revealed that they also play a role in functional biological processes.[2] Amyloids have also been invoked to be plausible early precursors to enzymes in the evolution of life, due to their ability to self-replicate and catalyse chemical reactions,[3,4] and nowadays they are emerging as promising building blocks for new supramolecular structures and advanced materials.[5] Amyloid fibrillar assemblies are characterized by a "cross-β" quaternary common structure, in which β-sheets are parallel to the fibril axis and their strands perpendicular to it.[6] This architecture is a robust supramolecular structure in which β-sheets come into contact forming a tightly packed solvent excluded core region, known steric zipper. Such architecture is stabilized by backbone hydrogen bonds between neighboring β-strands, and by other non-covalent interactions, such as π-π stacking, van der Waals, electrostatic and hydrophobic interactions. Final supramolecular structures[7] fall within to one of the eight classes of steric zippers and are driven by subtle changes in hydrophobicity, charge, and size of the peptides.

Several recent studies have revealed that amyloid architectures can provide scaffolds for enzyme-like catalysis.[8–12] In particular, the pioneering work of Korendovych et al.[12] showed that short seven-residue amyloid peptides can self-assemble and create active sites that are able to bind zinc and catalyze an esterase reaction, i.e. the hydrolysis of p-nitrophenylacetate (pNPA). These peptides exhibit alternating hydrophobic (Ile, Leu or Val) and polar (His) residues to create an amphiphilic β-strand that could further aggregate via hydrophobic interactions, while keeping His exposed to the solvent and interacting with Zn^{2+}. In addition, new peptides in which the His at position six is replaced by acidic (Asp, Glu), basic (Lys, Arg) and polar or aromatic (Gln, Tyr) residues were explored to evaluate how acid/bases from neighbouring side chains, serving as secondary ligands, influence the catalysis. Results showed a marked dependence on the nature of the residue at position six, the presence of Gln leading to the most active IHIHQH peptide, ($k_{cat}/K_M = 62\ M^{-1}\,s^{-1}$) The metal ion's proper coordination was shown also to be crucial, since a single His/Ala mutation resulted in an around 60-fold decrease in esterase activity. Importantly, catalytic activity correlated with the degree of assembly, monomeric peptides being essentially unable to catalyze this reaction.

Overall, results from these works indicate that the catalytic activity of these nanofibers is closely linked to their ability to self-assemble and produce the proper active sites within the three-dimensional fibrillar structure. Within this context, computational studies can provide very useful information to unravel the intricacies of such catalytic processes, including the influence of the sixth residue position. While Dong et al.[13] have contributed valuable insights into the molecular mechanisms driving esterase activity with amyloid fibers, the explicit role of the sixth position remains unaddressed.

[a] L. Roldan, L. Rodríguez-Santiago, J. Didier-Marechal, M. Sodupe
Departament de Química,
Edifici C, Universitat Autònoma de Barcelona,
Cerdanyola del Vallès 08193, Spain
E-mail: mariona.sodupe@uab.cat
luis.rodriguez.santiago@uab.cat

Supporting information for this article is available on the WWW under https://doi.org/10.1002/chem.202401797

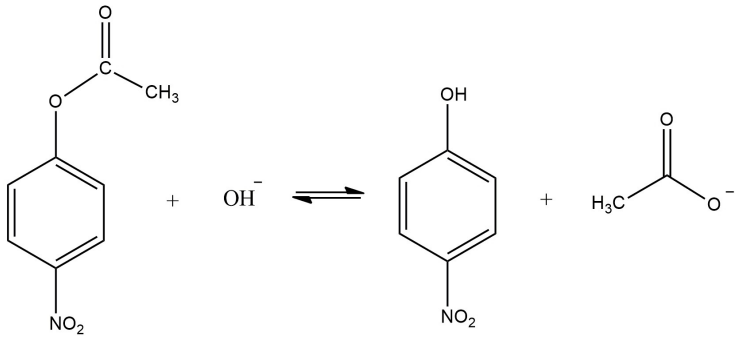

Scheme 1. Hydrolysis reaction of p-nitrophenylacetate.

This paper aims to provide a comprehensive computational study regarding the esterase activity of minimalist amyloid fibers, focusing on the role of the sixth residue position. Our investigation will encompass a detailed examination of the structural characteristics of IHIHIHI (IH7) and IHIHIQI (IH7Q) fibers, along with an exploration of the NPA hydrolysis reaction mechanism. Through this study, we aim to shed light on the intricate interplay between peptide sequence, structural arrangement, and catalytic function in amyloid-based enzymes.

Results and Discussion

As mentioned, Korendovych et al.[12] showed that minimalist amyloid fibres formed by seven residue amphiphilic peptides exhibit enzyme-like catalysis, particularly the hydrolysis of pNPA (Scheme 1), in the presence of Zn^{2+} ion.

The active sites reported at these Zn^{2+} -fibers mimic those in Zn^{2+}-metalloenzymes of carbonic anhydrase,[14–23] and exhibit the Zn^{2+} ion coordinated to three His and one OH^-, which originates from deprotonation of a water molecule, in a tetrahedral coordination. For these systems, deprotonation toward the deprotonated N of uncoordinated His has been estimated to have a ΔG of 4.3 kcal mol^{-1},[13] and is expected to be similar for both IH7 and IH7Q. Thus, from now on we will focus on the nucleophilic attack of the hydroxide ion bound to Zn^{2+} to pNPA, which leads to the formation of a tetrahedral oxyanion intermediate that subsequently evolves to p-nitrophenol and acetate (Scheme 1).

Experimental findings suggest that the catalytic process is influenced by the nature of the residue located at the sixth position of the fiber, with glutamine demonstrating the highest catalytic efficiency.[12] It has been hypothesized[13] that this specific residue might impact the fiber's twist angle, consequently altering the local environment of the active site. However, analysis conducted on the final 100 ns of the MD simulation of metal-bound fibers, once the system has achieved stability (Figure S1 of SI), reveals that the average twist angle between neighbour strands, as described in the computational methodology section, is similar in both Zn^{2+}-IH7 (12.4 ± 3.8) and Zn^{2+}-IH7Q (12.5 ± 5.0) fibers. A distribution of angles along the last 100 ns of the molecular dynamics simulations is provided in Figure S2 of the SI. Thus, the sixth position does not appear to induce notable variations in the fibre's twist angle that could influence its catalytic site and efficacy; for instance, by favouring the interaction of pNPA with two neighbours Zn^{2+} ions. Therefore, the most intriguing yet unresolved aspect remains how the sixth position of the fiber impacts its catalytic activity despite not being directly engaged in the Zn^{2+} binding.

Two working hypotheses based on the direct interaction between the sixth position and pNPA have been explored (Figure 1): i) the $-OCOCH_3$ ester group of pNPA or ii) the $-NO_2$ group of the pNPA interact with the residue in the sixth position. In both hypotheses, the side chain of the 6th residue would establish H-bond contacts between the proton donor group of Gln with the $-NO_2$ or $-OCOCH_3$ groups of pNPA, which could further activate the substrate favouring the OH^- nucleophilic attack, thereby enhancing the hydrolytic activity.

The main focus is to investigate the transient catalytic interactions of pNPA with its surrounding environment, particularly with the sixth residue. To achieve this, the pNPA substrate was docked using Gold software onto a central Zn^{2+} ion of the fiber, with at least 8 strands on each side. However, since preliminary quantum mechanics (QM) studies, considering only the active site, identified the oxyanion species resulting from the nucleophilic attack of OH^- on NPA as an intermediate in the hydrolysis process, this intermediate (Figure S3 of SI) was overlapped with the docked position of pNPA and parametrized in a bonded manner, so that MD simulations could be performed. PCA and RMSD values obtained for these pNPA-

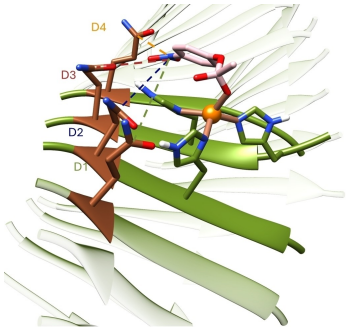

Figure 1. Potential interactions between the sixth residue of the heptapeptide and a) the $-OCOCH_3$ group and b) the $-NO_2$ group of pNPA for IH7Q.

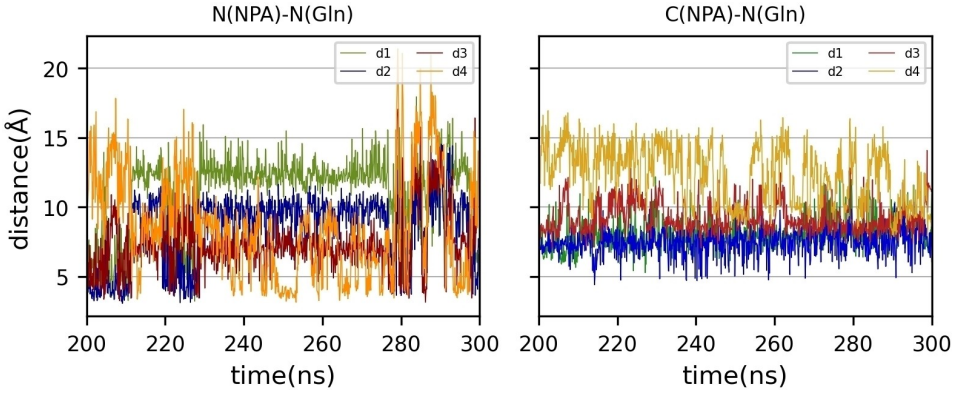

Figure 2. Intermolecular distances between the N atom of His (in IH7) and Gln (in IH7Q) of the 6th position and the N atom of $-NO_2$ (left) and C atom of $-OCOCH_3$ (right) of pNPA.

Zn^{2+}-IH7 and pNPA-Zn^{2+}-IH7Q simulations are given in Figure S4 of SI. This approach enables the simulation of potential interactions that may occur between the substrate and the surrounding environment.

To properly assess the interactions between pNPA and the sixth position, either from the same strand as the coordinating ion or the adjacent ones, the distances between the sixth residue and $-NO_2$ or $-COOCH_3$ groups of pNPA (Figure 1) were measured on the final 100 ns of the MD simulation. Such distances were determined by considering the N atom of NO_2 or the C atom of the ester group and the N atom of Gln (in IH7Q) and His (in IH7). According to QM calculations the threshold value was set to 5 Å. Values smaller than 5 Å indicate potential contacts that could influence the catalysis.

Figure 2 shows the intermolecular distances with the $-NO_2$ and $-COOCH_3$ groups of pNPA for both IH7 and IH7Q for the last 100 ns of the simulation. First, it can be observed that both for IH7 and IH7Q no suitable distances between the ester group and the sixth residue (Figure 2, right images) were identified, discarding our second hypothesis. Indeed, almost all along the trajectory the measured distances were larger than 5 Å thereby indicating that, if present, they should be weak, which is not expected to largely influence the catalysis. On the contrary, the $-NO_2$ group can reach feasible distances with the sixth position, particularly with Gln in IH7Q. Notably, contacts with Gln were present approximately 44% of the simulation time in IH7Q, compared to only 1% in IH7. Such difference arises from the length and nature of the side chain, which is larger and more flexible in Gln than in His.

The hypothesis of the interaction of the NO_2 from the pNPA substrate with the 6th position was then shown to be feasible. Consequently, ONIOM(QM/MM) calculations were performed to obtain the energy profile of the reaction for either IH7 and IH7Q, to describe the impact of the 6th residue on the catalysis. The starting geometry was, in both cases, a frame from MD simulations, in which pNPA was closest to the sixth residue. It should be noted that several possible orientations of pNPA, particularly of the $-OCOCH_3$ ester group concerning the metal ion, are possible. MD simulations have allowed us to select among them the most representative orientation exhibiting the C=O pointing toward Zn^{2+}.

Figure 3 depicts the Gibbs energy profiles of the hydrolysis of pNPA by IH7 and IH7Q as well as the optimized structures for the different stationary points obtained for IH7. Table 1 shows the relative energies of the different stationary points decomposed into the high-level and low-level contributions.

The first step of the reaction mechanism involves the nucleophilic attack of the Zn^{2+} coordinated OH^- to the C atom of the ester group of pNPA. As a result, an oxyanion coordinated to Zn^{2+} through the oxygen atom of C=O is obtained (Figure 3). This oxyanion complex presents Zn^{2+} tetracoordination as the O of the OH is replaced by the O from pNPA. The transition structure TS1, however, exhibits Zn^{2+} pentacoordination, with the N atoms of the three histidines, the O from the OH and the C=O from pNPA interacting with the metal cation. The computed energy barrier is $\Delta E^{\neq} = 13.0$ ($\Delta G^{\neq} = 17.3$) kcal mol^{-1} in terms of potential and Gibbs energy,

Table 1. Relative potential energies (ΔE) and Gibbs energies (ΔG) in gas phase and accounting for solvent corrections (ΔG_{sol}) (in kcal mol^{-1}) for the hydrolysis of pNPA in Zn^{2+}-IH7 and Zn^{2+}-IH7Q, decomposed into their high level (ΔE_{HL}) and low level (ΔE_{LL}) contributions.

	ΔE			ΔG	ΔG_{sol}
IH7	ΔE	ΔE_{HL}	ΔE_{LL}		
R	0.0	0.0	0.0	0.0	0.0
TS1	13.0	11.6	1.4	17.3	16.0
OA	1.8	0.4	1.4	7.8	2.8
TS2	9.8	8.1	1.7	13.9	−2.8
P	−22.4	−25.2	2.8	−19.5	−23.6
IH7Q					
R	0.0	0.0	0.0	0.0	0.0
TS1	11.3	9.3	2.0	14.6	14.2
OA	−2.2	−5.1	2.9	2.0	0.6
TS2	4.1	3.3	0.9	5.6	−5.6
P	−29.5	−25.5	−4.0	−28.6	−30.7

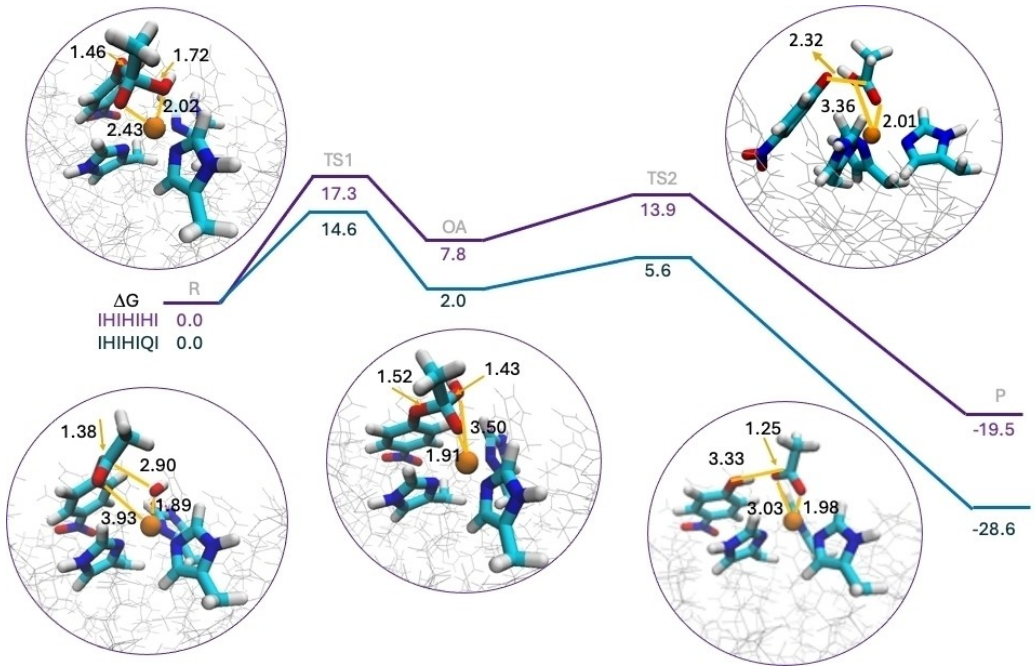

Figure 3. Gibbs energy profiles for pNPA hydrolysis at the surface of IH7 (in purple) and IH7Q (in blue). R stands for reactants, OA for oxyanion and P for products. Optimized structures for the different stationary points obtained for IH7. Distances are in Å and relative energies in kcal mol^{-1}

respectively. Along this process, the C–O bond distance of NPA moiety significantly increases from 1.38 Å in NPA to 1.52 Å in the oxyanion (Figure 3). From this oxyanion intermediate, the proton of OH is transferred to the O^- of the nascent nitrophenolate, through an energy barrier of $\Delta E^{\neq} = 8.0$ ($\Delta G^{\neq} = 6.1$) kcal mol^{-1} (Table 1, Figure 3, TS2), which leads to the final products nitrophenol and acetate, the latter one being coordinated to Zn^{2+} (P in Figure 3). The computed overall Gibbs reaction energy (−19.5 kcal mol^{-1}) indicates that the reaction is highly exergonic. Interestingly, this mechanism differs slightly from that reported by Dong et al.[13] in which the oxyanion evolves toward acetic acid and nitrophenolate, which further converts to nitrophenol and acetate through an additional proton transfer.

Decomposing the relative energies into their high level and low-level components shows that, as expected, the energy profile is mainly dictated by the high-level part enclosing the active site. The low-level part, while non-negligible, is destabilizing accounting for 2–3 kcal mol^{-1} of the total relative energies. Furthermore, the inclusion of solvents effects through the SMD implicit solvent model for the high-level region makes the reaction more exergonic and makes TS2 more stable than the OA, so that products would be obtained directly in a one-step process.

For IH7Q, a similar energy profile as that of IH7 is obtained (Figure 3, blue), albeit with lower Gibbs energy barriers (14.6 *vs* 17.3 kcal mol^{-1} for TS1 and 3.6 *vs* 6.1 kcal mol^{-1} for TS2, with respect to OA). Similarly to IH7, TS1 exhibits Zn^{2+} pentacoordination with the O of pNPA at 2.38 Å and that of OH at 2.03 Å (Figure 4), while the oxyanion OA shows Zn^{2+} tetracoordination as the O from OH is displaced by the O of pNPA. Notably, the reaction energy indicates that the process is significantly more exergonic for IH7Q (−28.6 kcal mol^{-1}) than for IH7 (−19.5 kcal mol^{-1}), in line with the smaller energy barriers for the former. Furthermore, the decomposition of relative energies into their high-level and low-level contributions (Table 1) indicates that, as for IH7, the low-level part is destabilizing by 2–3 kcal mol^{-1}, except for the products for which a stabilizing contribution of 4 kcal mol^{-1} is detected.

As for IH7, solvent effects make the reaction more exergonic and stabilizes TS2, which becomes lower in energy than the OA. These changes do not modify the previously obtained trends, the Gibbs energy barrier of IH7Q being smaller than that of IH7 (14.2 vs 16 kcal mol^{-1}). Such differences in the energetic barriers of IH7 and IH7Q may explain the enhanced catalytic activity observed experimentally for the latter, which could be attributed to the polarizing effect of Gln on pNPA. Indeed, a detailed analysis of the structure of IH7 and IH7Q transition structures indicates that Gln can stablish stabilizing H-bond contacts with NPA along the reaction. Figure 4 displays the optimized structures of TS1 and the products. Remaining structures are given in Figure S5 of SI.

In TS1, the lateral chain of Gln (–CH_2–CH_2–CO–NH_2) is acting both as a proton acceptor through the CO group and as proton donor through NH_2. The CO establishes a H-bond contact with the imidazole N–H of one of the Zn^{2+} coordinating His at 1.74 Å, while –NH_2 acts as proton donor and interacts with –NO_2, with a H-bond distance of 2.15 Å. In the products, the hydrogen bond of the –NH imidazole with CO remains similar (1.80 Å), however, the –NH_2···–NO_2 H-bond strengthens significantly, the measured distance decreasing up to 1.95 Å. Overall, this structure exhibit a network of hydrogen bonds that involves the two products of the reaction and the active site, which likely contributes to the larger exergonicity of the

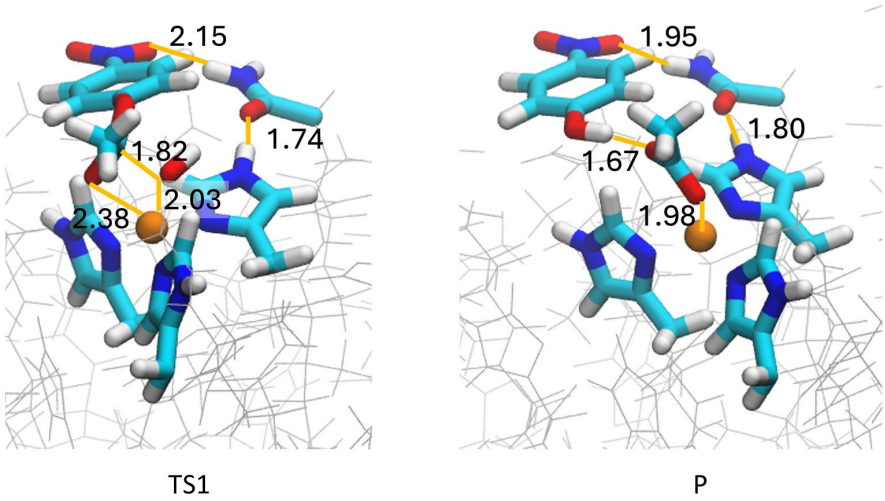

Figure 4. Main geometrical features and contacts for the optimized transition structure TS1 and products P for IH7Q. Distances in Å.

reaction and the smaller energy barriers observed for IH7Q compared to IH7, for which such contacts are essentially absent. Although results can be sensitive to the starting structure extracted from molecular dynamics, the frame considered to explore the mechanism is representative since it belongs to one of the most populated clusters.

Overall, and as found in the work of Dong et. al.[13] the rate determining step of the whole reaction is the nucleophilic attack. For IH7Q, our computed energy barrier $\Delta G^{\neq}$ value for this step is 14.2 kcal mol^{-1}, in reasonable agreement with that reported in ref.[13] (22.15 kcal mol^{-1}), if one considers that this latter value also includes the 4.3 kcal mol^{-1} energy cost for water deprotonation. Differences with previous work[13] can be attributed to the different models used in the study of the reaction mechanism. In the work of Dong et. al. the mechanistic QM study is done considering only the two strands of the active site and restricting the backbone geometry to that found for a representative structure in the 16-strand fiber molecular dynamic's simulations, while present work includes the whole 40-strand fiber at the QM/MM level, and no restrictions are imposed. Furthermore, in the reaction mechanism study, the work of Dong et al. includes three additional water molecules besides the one coordinated to the Zn^{2+} ion, while present work addresses solvent effects with an implicit solvent model.

Finally, it should be mentioned that while present work provides a plausible explanation for the enhanced catalytic activity of IH7Q compared to IH7, other effects such as the role of explicit water molecules, the stability of the fibre, or polymorphism should also be addressed to fully understand this complex catalytic process.

Conclusions

The present work addresses the esterase activity exhibited by minimalist amyloid fibers composed of short seven-residue peptides. It seeks to understand the underlying molecular mechanisms driving catalysis in these amyloid-based enzymes, mainly focusing on the role of the sixth residue position by means of computational methods. Contrary to the initial hypotheses, computational analysis revealed that the twist angle of the fiber and thus, the catalytic site's environment, is not notably affected by the sixth residue. Instead, the study unveiled that the sixth residue interacts with the pNPA substrate, particularly its $-NO_2$ group, potentially enhancing catalysis, as observed experimentally.[12] Molecular dynamics demonstrated the feasibility of interactions between the $-NO_2$ group of pNPA and the sixth residue, with glutamine (Gln) exhibiting significantly frequent and strong contacts, as compared to histidine (His) for which such contacts are essentially absent. This finding as well as QM/MM simulations of the reaction mechanism suggests that interaction with Gln enhances catalytic activity through the formation of a stabilizing network of H-bond interactions with pNPA that leads to lower energy barriers and a more exergonic reaction. Such contacts appear to be particularly effective for Gln due to the larger and more flexible lateral chain in Gln compared to His. This finding underscores the significance of subtle molecular interactions in modulating catalytic efficiency and provides valuable insights into the intricate interplay between peptide sequence, structural arrangement, and catalytic function in amyloid-based enzymes, offering potential avenues for the design and optimization of bioinspired amyloid catalysts.

Computational Details

Models. Initial models were built, as in previous studies,[10,24,25] with an in-house script[26] which allows obtaining a starting three-dimensional structure of steric zippers models by specifying the composition of the peptide and a set of geometric parameters: the number of strands, the separation between strands in each β-sheet, the number of layers and the separation among the layers. The N-terminus was acetylated and the C-terminus amidated to match exactly the experimental composition.

Based on already reported works, the structures of IH7 and IH7Q,[27] were assumed to exhibit a parallel packing of β-strands within each

sheet and an antiparallel packing between sheets (Class 1 of steric zippers).[7] The length of each β-sheet was set to 20 strands, so that each model is composed of 40 strands for the bilayers (Figure 5).

Molecular Dynamics simulations. Classical Molecular Dynamics simulations were carried out to define the effect of the sixth position on the structures' twist angle. Once a stable structure for each sequence was obtained, Zn^{2+} and pNPA dockings were performed. Docking of the Zn^{2+} ion was performed on the most populated cluster of the fibrils. Such docking calculations were carried out with the GOLD program[28] using the GoldScore scoring[29] function, with modified parameters to include possible coordination of metal ions.[30] Genetic algorithm (GA) parameters were set to 50 GA runs and a minimum of 100,000 operations each. All histidines were deprotonated and full flexibility allowed for this calculation, to allow the system to coordinate Zn^{2+} ion with the most suitable nitrogen from His. In a full-coverage model, with the maximum number of Zn^{2+} coordinating to three surface histidines, two of the three coordinating His per metallic site should be double deprotonated since they would be involved in the coordination of two neighbour Zn^{2+} (pdb 5UGK). This situation cannot be parametrized with MCPB.py,[31] since it would require considering the whole fibre for calculating charge distribution, instead of a limited coordination sphere. Therefore, we considered a half-coverage model, in which all coordinating His are singly protonated. For such half-coverage model, docking calculations found a compatible coordination sphere, consisting of three coordinating histidines (2 His from strand i, one coordinating through Nδ and another one through Nε, and 1 His from strand i + 1, through Nδ), in accordance with results derived from experimental data (Figure 5).[27] A hydroxide would complete the tetrahedral coordination environment of the active site.

Once Zn^{2+} coordination was determined, the pNPA susbtrate was docked over the $(His)_3Zn^{2+}$-OH^- catalytic site, and the obtained coordinated complexes were again submitted to MD simulations, to analyse the substrate's most recurrent position concerning the environment.

Zn^{2+} metal parameters were obtained using the MCPB.py Amber tool,[31] from quantum mechanical calculations with DFT(B3LYP)[32] and adding Grimme's D3[33] correction for dispersion. The coordinated structure was optimized with the 6–31 + G(d,p) basis for C, H, N and O atoms, and the Stuttgart ECP and associated basis set for Zn.[34] Solvent effects were accounted for with the solvent-polarizable dielectric continuum model (SMD) in water.[35] Force constants and equilibrium parameters for those atoms coordinating the metal ion were obtained using the Seminario method,[36] while point charges were derived using the RESP[37] (restrained electrostatic potential) model. pNPA parametrization was performed with GAFF. The complex was solvated within a cubic box of pre-equilibrated TIP3P water molecules and Cl^- ions to balance the total charge according to the needs of each system.

Molecular Dynamics simulations were done for a minimum of 300 ns with the Amber suite using the ff14SB[38,39] force field in the NPT ensemble, using an integration time step of 1 fs. Such force field was used in our previous studies providing good results when compared to an experimentally resolved validation set.[25] Constant temperature and pressure were set by coupling the system to a Monte Carlo barostat at 1.01325 bar and a Langevin thermostat at 300 K. The SHAKE[40] algorithm was used to constrain hydrogen atoms bonds.

Analysis. Principal Component Analysis (PCA),[41] RMSD and clustering were performed over the MD simulations to ensure that thorough conformational sampling is achieved. The twist angle is computed as the angle between the vectors defined by the acetylated N-terminus and the amidated C-terminus of consecutive strands. The twist angle of the fiber is then determined as the average value of all these angles, considering both the upper and bottom layers, over the last 100 ns of the simulation. In addition, the distances of both $-NO_2$ and $-OCOCH_3$ groups of the pNPA substrate with the amide nitrogen of Gln were analysed.

QM/MM calculations. The reaction mechanism was investigated through ONIOM QM/MM calculations[42] with the Gaussian 16 code.[43] These simulations were analysed using the MolUp plug-in for VMD.[44] The QM region included the metal, the ligand, and the three coordinated His residues up to the Cβ atom. The rest of the system (MM region) comprised over 5000 atoms. The energy of the QM region was calculated with the B3LYP functional[32] and Grimme's D3 correction for dispersion,[33] using the 6–31 + G(d,p) basis set[45] for main elements and the Stuttgart ECP pseudopotential and associated basis set for Zn,[34] in gas phase. Solvent effects for the QM region were accounted for with the SMD implicit model at the gas phase optimized geometries. The MM part of the system was treated with AMBER FF19SB.[46] The nature of all stationary points was verified by vibrational analysis, to ensure that all frequencies are positive in the minima and that only one frequency is negative in the transition structures.

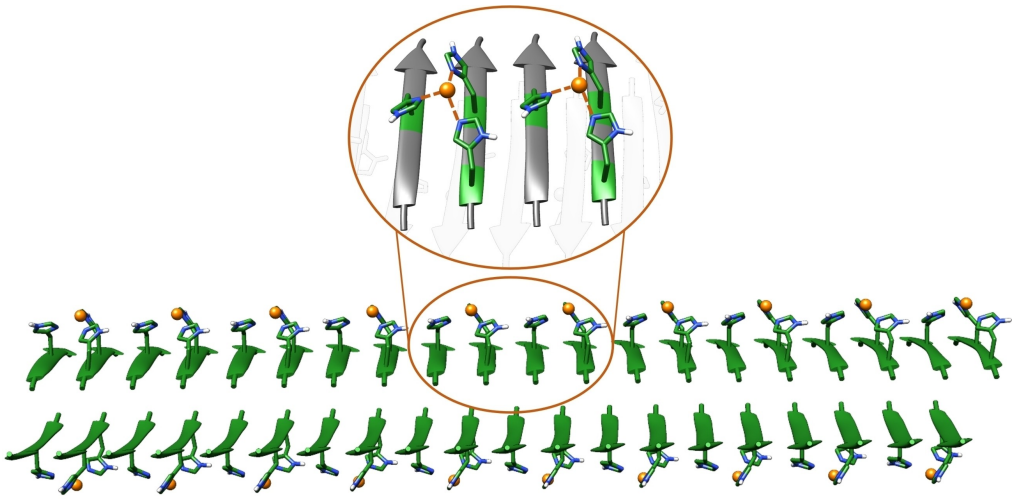

Figure 5. Half coverage model of Zn^{2+} coordination with IH7, with three His forming the coordination sphere (2 with Nδ and 1 with Nε).

Acknowledgements

This work was supported by the projects PID2020-116861GB-I00 and PID2020-112715GB-I00 from the Spanish Ministerio de Ciencia y Educación. LR would like to thank Generalitat de Catalunya (grant 2020FI_B2_01000). We thank F. Peccati and G. Jiménez-Osés for fruitful discussions.

Conflict of Interests

The authors declare no conflict of interest.

Data Availability Statement

The data that support the findings of this study are available in the supplementary material of this article.

Keywords: Esterase activity · Catalysis · Amyloid fibers · QM/MM · DFT

[1] P. C. Ke, R. Zhou, L. C. Serpell, R. Riek, T. P. J. Knowles, H. A. Lashuel, E. Gazit, I. W. Hamley, T. P. Davis, M. Fändrich, D. E. Otzen, M. R. Chapman, C. M. Dobson, D. S. Eisenberg, R. Mezzenga, *Chem. Soc. Rev.* **2020**, *49*, 5473–5509.
[2] D. Otzen, R. Riek, *Cold Spring Harb. Perspect. Med.* **2019**, *11*, a033860.
[3] O. Zozulia, M. A. Dolan, I. V. Korendovych, *Chem. Soc. Rev.* **2018**, *47*, 3621–3639.
[4] J. Greenwald, W. Kwiatkowski, R. Riek, *J. Mol. Biol.* **2018**, *430*, 3735–3750.
[5] M. Díaz-Caballero, M. R. Fernández, S. Navarro, S. Ventura, *Prion* **2018**, *12*, 266–272.
[6] R. Nelson, M. R. Sawaya, M. Balbirnie, A. Madsen, C. Riekel, R. Grothe, D. Eisenberg, *Nature* **2005**, *435*, 773–778.
[7] M. R. Sawaya, S. Sambashivan, R. Nelson, M. I. Ivanova, S. A. Sievers, M. I. Apostol, M. J. Thompson, M. Balbirnie, J. J. W. Wiltzius, H. T. McFarlane, A. Ø. Madsen, C. Riekel, D. Eisenberg, *Nature* **2007**, *447*, 453–457.
[8] Z. S. Al-Garawi, B. A. McIntosh, D. Neill-Hall, A. A. Hatimy, S. M. Sweet, M. C. Bagley, L. C. Serpell, *Nanoscale* **2017**, *9*, 10773–10783.
[9] O. V. Makhlynets, P. M. Gosavi, I. V. Korendovych, *Angewandte Chemie* **2016**, *128*, 9163–9166.
[10] M. Díaz-Caballero, S. Navarro, M. Nuez-Martínez, F. Peccati, L. Rodríguez-Santiago, M. Sodupe, F. Teixidor, S. Ventura, *ACS Catal.* **2021**, *11*, 595–607.
[11] S. Navarro, M. Díaz-Caballero, F. Peccati, L. Roldán-Martín, M. Sodupe, S. Ventura, *ACS Nano* **2023**, *17*, 16968–16979.
[12] C. M. Rufo, Y. S. Moroz, O. V. Moroz, J. Stöhr, T. A. Smith, X. Hu, W. F. DeGrado, I. V. Korendovych, *Nat. Chem.* **2014**, *6*, 303–309.
[13] R. Song, X. Wu, B. Xue, Y. Yang, W. Huang, G. Zeng, J. Wang, W. Li, Y. Cao, W. Wang, J. Lu, H. Dong, *J. Am. Chem. Soc.* **2019**, *141*, 223–231.
[14] D. Riccardi, S. Yang, Q. Cui, *Biochimica et Biophysica Acta (BBA) - Proteins and Proteomics* **2010**, *1804*, 342–351.
[15] Z. Smedarchina, W. Siebrand, A. Fernández-Ramos, Q. Cui, *J. Am. Chem. Soc.* **2003**, *125*, 243–251.
[16] D. Riccardi, Q. Cui, *J. Phys. Chem. A* **2007**, *111*, 5703–5711.
[17] Q. Cui, M. Karplus, *J. Phys. Chem. B* **2003**, *107*, 1071–1078.
[18] A. Bottoni, C. Z. Lanza, G. P. Miscione, D. Spinelli, *J. Am. Chem. Soc.* **2004**, *126*, 1542–1550.
[19] H. Shimahara, T. Yoshida, Y. Shibata, M. Shimizu, Y. Kyogoku, F. Sakiyama, T. Nakazawa, S. Tate, S. Ohki, T. Kato, H. Moriyama, K. Kishida, Y. Tano, T. Ohkubo, Y. Kobayashi, *J. Biol. Chem.* **2007**, *282*, 9646–9656.
[20] B. Sjöblom, M. Polentarutti, K. Djinović-Carugo, *Proc. Nat. Acad. Sci.* **2009**, *106*, 10609–10613.
[21] W. Sattler, G. Parkin, *Chem. Sci.* **2012**, *3*, 2015.
[22] D. Jiao, S. B. Rempe, *Biochemistry* **2012**, *51*, 5979–5989.
[23] V. Hakkim, V. Subramanian, *J. Phys. Chem. A* **2010**, *114*, 7952–7959.
[24] F. Peccati, M. Sodupe, *J. Chem. Phys.* **2021**, *155*, 055101.
[25] F. Peccati, M. Díaz-Caballero, S. Navarro, L. Rodríguez-Santiago, S. Ventura, M. Sodupe, *Chem. Sci.* **2020**, *11*, 13143–13151.
[26] F. Peccati, fibTool https://github.com/insilichem/catalytic amyloids (accessed Jul 2, 2024).
[27] M. Lee, T. Wang, O. V. Makhlynets, Y. Wu, N. F. Polizzi, H. Wu, P. M. Gosavi, J. Stöhr, I. V. Korendovych, W. F. DeGrado, M. Hong, *Proc. Nat. Acad. Sci.* **2017**, *114*, 6191–6196.
[28] G. Jones, P. Willett, R. C. Glen, A. R. Leach, R. Taylor, *J. Mol. Biol.* **1997**, *267*, 727–748.
[29] G. Jones, P. Willett, R. C. Glen, *J. Mol. Biol.* **1995**, *245*, 43–53.
[30] G. Sciortino, J. Rodríguez-Guerra Pedregal, A. Lledós, E. Garribba, J. D. Maréchal, *J. Comput. Chem.* **2018**, *39*, 42–51.
[31] P. Li, K. M. Merz, *J. Chem. Inf. Model.* **2016**, *56*, 599–604.
[32] A. D. Becke, *J. Chem. Phys.* **1993**, *98*, 5648–5652.
[33] S. Grimme, J. Antony, S. Ehrlich, H. Krieg, *J. Chem. Phys.* **2010**, *132*, 154104.
[34] M. Dolg, U. Wedig, H. Stoll, H. Preuss, *J. Chem. Phys.* **1987**, *86*, 866–872.
[35] A. V. Marenich, C. J. Cramer, D. G. Truhlar, *J. Phys. Chem. B* **2009**, *113*, 6378–6396.
[36] J. Seminario, *Int. J. Quantum Chem.* **1996**, *60*, 1271–1277.
[37] C. I. Bayly, P. Cieplak, W. D. Cornell, P. A. Kollman, *J. Phys. Chem.* **1993**, *97*, 10269–10280.
[38] D.A. Case, K. Belfon, I.Y. Ben-Shalom, S.R. Brozell, D.S. Cerutti, T.E. Cheatham, III, V.W.D. Cruzeiro, T.A. Darden, R.E. Duke, G. Giambasu, M.K. Gilson, H. Gohlke, A.W. Goetz,R Harris, S. Izadi, S.A. Izmailov, K. Kasavajhala, A. Kovalenko, R. Krasny, T. Kurtzman, T.S. Lee, S. LeGrand, P. Li, C. Lin, J. Liu, T. Luchko, R. Luo, V. Man, K.M. Merz, Y. Miao, O. Mikhailovskii, G. Monard, H. Nguyen, A. Onufriev, F. Pan, S. Pantano, R. Qi, D.R. Roe, A. Roitberg, C. Sagui, S. Schott-Verdugo, J. Shen, C.L. Simmerling, N.R. Skrynnikov, J. Smith, J. Swails, R.C. Walker, J. Wang, L. Wilson, R.M. Wolf, X. Wu, Y. Xiong, Y. Xue, D.M. York and P.A. Kollman (2020), AMBER 2020, University of California, San Francisco.
[39] J. A. Maier, C. Martinez, K. Kasavajhala, L. Wickstrom, K. E. Hauser, C. Simmerling, *J. Chem. Theory. Comput.* **2015**, *11*, 3696–3713.
[40] R. Elber, A. P. Ruymgaart, B. Hess, *Eur. Phys. J. Spec. Top.* **2011**, *200*, 211–223.
[41] S. Wold, K. Esbensen, P. Geladi, *Chemometr. Intell. Lab. Syst.* **1987**, *2*, 37–52.
[42] L. W. Chung, W. M. C. Sameera, R. Ramozzi, A. J. Page, M. Hatanaka, G. P. Petrova, T. V. Harris, X. Li, Z. Ke, F. Liu, H.-B. Li, L. Ding, K. Morokuma, *Chem. Rev.* **2015**, *115*, 5678–5796.
[43] Gaussian 16, Revision C.01, M. J. Frisch, G. W. Trucks, H. B. Schlegel, G. E. Scuseria, M. A. Robb, J. R. Cheeseman, G. Scalmani, V. Barone, G. A. Petersson, H. Nakatsuji, X. Li, M. Caricato, A. V. Marenich, J. Bloino, B. G. Janesko, R. Gomperts, B. Mennucci, H. P. Hratchian, J. V. Ortiz, A. F. Izmaylov, J. L. Sonnenberg, D. Williams-Young, F. Ding, F. Lipparini, F. Egidi, J. Goings, B. Peng, A. Petrone, T. Henderson, D. Ranasinghe, V. G. Zakrzewski, J. Gao, N. Rega, G. Zheng, W. Liang, M. Hada, M. Ehara, K. Toyota, R. Fukuda, J. Hasegawa, M. Ishida, T. Nakajima, Y. Honda, O. Kitao, H. Nakai, T. Vreven, K. Throssell, J. A. Montgomery, Jr., J. E. Peralta, F. Ogliaro, M. J. Bearpark, J. J. Heyd, E. N. Brothers, K. N. Kudin, V. N. Staroverov, T. A. Keith, R. Kobayashi, J. Normand, K. Raghavachari, A. P. Rendell, J. C. Burant, S. S. Iyengar, J. Tomasi, M. Cossi, J. M. Millam, M. Klene, C. Adamo, R. Cammi, J. W. Ochterski, R. L. Martin, K. Morokuma, O. Farkas, J. B. Foresman, and D. J. Fox, Gaussian, Inc., Wallingford CT, 2016.
[44] H. S. Fernandes, M. J. Ramos, M. F. S. A. Cerqueira, *J. Comput. Chem.* **2018**, *39*, 1344–1353.
[45] V. A. Rassolov, M. A. Ratner, J. A. Pople, P. C. Redfern, L. A. Curtiss, *J. Comput. Chem.* **2001**, *22*, 976–984.
[46] C. Tian, K. Kasavajhala, K. A. A. Belfon, L. Raguette, H. Huang, A. N. Migues, J. Bickel, Y. Wang, J. Pincay, Q. Wu, C. Simmerling, *J. Chem. Theory Comput.* **2020**, *16*, 528–552.

Manuscript received: May 7, 2024
Accepted manuscript online: July 8, 2024
Version of record online: August 20, 2024